Article

Exploring the Potential of Amino-Functionalized Zeolite Series/H₃PO₄-Biochar for Environmental Microplastic Removal

Martins O. Omorogie* and Brigitte Helmreich

Cite This: *Ind. Eng. Chem. Res.* 2024, 63, 3947−3961

Read Online

ACCESS | Metrics & More | Article Recommendations | Supporting Information

ABSTRACT: The problem of microplastics (MPs) in the environment has been an emerging concern to the world in recent times. This is because the migration of MPs in the environment has been identified as deleterious culprits of the entire ecosystem and by extension may cause a decrease in life expectancy and quality of life in humans, fauna, and flora. This threat is seriously militating against the continuous existence and well-being of the entire ecosystem. Therefore, this research attempts to provide a solution to this global problem through the application of amino-functionalized zeolite series/phosphoric acid-coffee waste biochar (AFZ) for the removal of polystyrene MPs in solutions, drinking water, and wastewater. Findings from this research showed that AFZ removed 4.78 to 4.85 mg g^{-1} of polystyrene MPs from solutions at 20 to 50 °C, respectively. This was achieved by a combination of chemisorption and physisorption mechanisms via hydrophobic interactions between the π-electrons of the sp^2 carbon orbital and $\pi-\pi$ aromatic moieties of AFZ and the π-electrons of the polystyrene MPs and electrostatic attraction between AFZ and polystyrene MPs, respectively. Surface characterization of AFZ before and after its uptake of polystyrene MPs revealed that functional moieties such as C−H, C−O, C=C, N−H, Al−O, and Si−O was majorly responsible for the adsorption process. Hence, this research revealed that AFZ has potential to treat polystyrene MP-contaminated drinking water and wastewater.
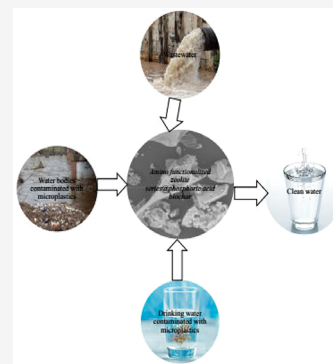
1.0. INTRODUCTION

Microplastics (MPs) are emerging contaminants that have posed a deleterious menace to the environment in recent times. Technological advancement and globalization, which have led to the quantum applications of plastic products in all spheres of human endeavors, have tremendously increased MP pollution in the ecosystem.[1,2] Due to the alarming utilization of plastics (poly(ethylene), poly(propylene), poly(styrene), poly(methyl metacrylate), poly(ethylene terephthalate), poly(amide), *etc.*) all over the world, statistical data from Plastics Europe (Consortium of European Plastic Producers) has shown that global plastic production in 2020 has risen to 367 million tons, and it is expected to rise to 445 million tons by 2025.[3,4] This statistical data are expected to increase by 29% in the year 2028.[5] Developing efficient strategies for the consumption and sustainable production of plastics have become an issue of utmost and imperative importance if a lasting solution must be sought to this environmental quagmire currently ravaging the world.[6] The global plastic production comprises approximately 77% of polymers with a carbon−carbon skeleton, having molecular structures and moieties that have strong resistance to environmental degradation, thus resulting in long-lasting chemical compounds and their reactive intermediates that persist in the environment for decades.[7,8] The pathways of MPs into the environment are by steady disintegration into tiny particles under the influence of weathering, mechanical wear, solar radiation, and microbes.[9,10] These environmental recalcitrance, chemical stability, unique persistence, and nonbiodegradability of MPs have led to precarious toxicological impacts and the continuous survival of humans, aquatic biota, flora, and fauna.[1]

The fragments of plastics are widely distributed in various water sources, such as drinking water, wastewater treatment plants (WWTPs), groundwater, sewage drains, fresh water, sediments, lakes, rivers, oceans, estuaries, atmosphere, soil, food, humans, animals, and aquatic lives.[11−16] Moreover, the physicochemical properties of MPs such as their high surface area, small particle size, and strong hydrophobicity make them special carriers for the transport or migration of other toxic contaminants, which comprise pathogens, plasticizers, antibiotics, pesticides, pharmaceuticals, and heavy metals.[14]

MPs in the environment have become a serious concern to the global scientific community. The effective removals of MPs present in drinking water, wastewater, and sewage drains are problems of contemporary concern to researchers, government, and environmental policy makers globally.[1,3,7,12]

An avalanche of technologies has been used to remove MPs from water, such as biological processes (microbial degrada-

tion), advanced oxidation processes (photocatalysis, photo-electrocatalysis, electrocatalysis, and electrocoagulation), other chemical-physical processes (coagulation and adsorption), and mechanical or physical processes (membrane filtration, density concentration, magnetic extraction, and magnetic separation). These technologies have different pitfalls, which include increased amounts of coagulants, pore blockage of membranes, low efficiency, nonsimplicity, expensive processability, to mention a few. Among these technologies, adsorption technology is the simplistic, efficient, and cost-effective technology applied for water treatment due to the fact that it minimizes reactive chemical intermediates and secondary byproducts, no special technique is needed, and it is effective. In recent times, few publications are available in literature for the application of adsorption technology for the removal of MPs in water.[17−30]

It is interesting to note that MPs have been detected in human placentas and blood, respiratory and digestive tracts of aquatic species, and drinking water sources.[14] The health hazards of the accumulation of MPs in human, animals, and aquatic lives could lead to neurotoxicity, impaired development, oxidative stress, intestinal injuries, and a wide array of inflammation. The human health and ecological impacts of MPs contamination has become an issue of serious concern to the world, as the global production of plastics is on the rise.[14,31,32] MPs, which are contaminants of emerging concern in water, have been promoting damage to the ecosystem in recent times. Hence, rapid and urgent attention has to be given to this life-threatening problem so as to proffer a swift panacea to this global problem and prevent further damage being done to the ecosystem in the future. An avalanche of research works in literature show that various attempts that have been made to solve this problem have been limited to the application of various MPs to remove other contaminants such as non-organics, organics and microbes in water.[33−54] Also, these attempts have shown that these MP adsorbents have the potential to leach into treated water, thereby escalating this problem.

To date, few research works are available in literature that reported the application of adsorbents for the removal of MPs from contaminated water.[17−24,30,55,56] These adsorbents utilized in the literature are expensive and readily unavailable and thus may cause limitations in their usage. This study addressed this pitfall such that a low-cost adsorbent from a cheap and ubiquitous source was used for the removal of polystyrene monodispersed microsphere suspensions (PSMMs) from contaminated water.

The application of amino-functionalized zeolite series/H$_3$PO$_4$-coffee waste biochar for the removal of PSMMs in wastewater and drinking water might provide a potential solution to this environmental problem.

2.0. MATERIALS AND METHODOLOGY

All chemicals were obtained from commercial sources and used without further purification.

2.1. Preparation of the Adsorption Material (Amino-Functionalized Zeolite Series/H$_3$PO$_4$-Biochar). In the first step, 85% phosphoric acid (*ortho*-phosphoric acid, H$_3$PO$_4$) (Merck, KGaA, Germany) was added in a stepwise sequence to deionized water (Millipore, electrical resistivity of 18.2 MΩ cm at 23.4 °C) in the ratio 1:3. Thereafter, 50 g of coffee waste (as dry mass) was added to 720 mL of H$_3$PO$_4$ solution and soaked for 21 h to allow its proper H$_3$PO$_4$ impregnation. Then, the

coffee waste-H$_3$PO$_4$ suspension was filtered under vacuum to obtain a wet residue of H$_3$PO$_4$-impregnated coffee waste, which was oven-dried at 105 °C for 24 h in an oven (ThermoFisher Scientific GmbH, Germany). The dry mass H$_3$PO$_4$-impregnated coffee waste obtained was crushed with a mortar and pestle into "dark powder".

In the second step, 20 g of the dark powder, 5 g of ammonium ZSM-5 (Zeolite Socony Mobile-5) zeolite (National Institute of Standard and Technology, USA), and 5 g of zeolite Y (Merck, KGaA, Germany) were added together and mechanically mixed with a mortar and pestle to obtain a uniform mixture. This uniform mixture was transferred into crucibles that were heated (annealed) in a muffle furnace (Carbolite, CWF 1100 Model (Merck, KGaA, Germany) at 550 °C for 2.5 h at a heating rate (annealing rate) of 30 °C min^{-1}. After heating (annealing), the resulting "amino-functionalized zeolite series/H$_3$PO$_4$-biochar" was allowed to cool to room temperature before it was removed from the furnace and stored in a desiccator for experimental use.

2.2. Preparation of Polystyrene (PS) Monodispersed Microsphere Suspension. The analytical standard of 6 μm monodispersed polystyrene (PS) microsphere suspension with a specific gravity of 1.05 g cm^{-3} (Sigma-Aldrich Chemie GmbH, Germany) was sonicated in an ultrasonic bath (Bandelin Electronic GmbH & Co. KG, Germany) for 15 min so as to enhance their dispersion in a 1:1 deionized water/ethanol mixture. After sonication, the standard solution of PS monodispersed microsphere suspension (PSMMs) was diluted into various experimental concentrations.

2.3. Adsorption and Desorption Studies. For the adsorption studies (each in triplicate), 50 mg each of amino-functionalized zeolite series/H$_3$PO$_4$-biochar (AFZ) was added to 25 mL of 10 mg·L^{-1} PSMMs and agitated for 3 h at 200 rpm, within the pH range of 1.0 to 13.0 (pH studies), 1 to 10 mg·L^{-1} (equilibrium studies), 1 to 180 min (kinetic studies), 20 to 50 °C (thermodynamic studies), and 0.05 to 1.25 g (adsorbent dose).

Recycle study was done for AFZ using solvents, such as HNO$_3$, acetone, deionized water, and ethanol, for 3 h at 200 rpm for six cycles at 20 °C. Additionally, samples of drinking water (DW) and wastewater (WW) from WW Treatment Plant in Garching (48° 15′N 11° 39′E), Germany, were collected and spiked with 1, 4, and 10 mg·L^{-1} PSMMs. Fifty milligrams of AFZ was added to 25 mL of these spiked solutions and agitated for 3 h at 200 rpm. The WW was characterized by chemical oxygen demand (COD), biochemical oxygen demand in 5 days (BOD$_5$), total dissolved solids (TDS), total suspended solids (TSS), electrical conductivity (EC), and turbidity.

After all experiments, samples were centrifuged (Multi-application Centrifuge, NUWND Model, Germany) for 10 min at 3000 rpm to get their supernatants. These supernatants were analyzed for the residual concentrations of PSMMs by a UV/Visible Spectrophotometer (DR 6000 Model, Hach Lange GmbH, Düsseldorf, Germany).

The amount of PSMMs adsorbed (Q_e) in mg per g of AFZ was calculated by the mass balance equation, given as

$$Q_e = \left\{ \left(C_i - C_e \right) \times \frac{V}{M} \right\} \tag{1}$$

C_i, C_e, V, and M in eq 1 are expressed as the initial concentration of adsorbate ions (mg·L^{-1}), equilibrium

concentration of adsorbate ions (mg·L^{-1}), volume of aqueous solutions (L), and mass of adsorbent (g), respectively.

Also, the experimental data obtained from equilibrium, kinetic, and thermodynamic studies were fit into two-parameter[57] and three-parameter nonlinear equations,[58] optimized by the Quasi-Newton least-squares algorithm, sum of square error (SSE), and correlation coefficient (R^2) in a KyPlot Software 2.0 model (KyensLab Incorporated, Tokyo, Japan) and Data Analysis and Graphing Software, OriginPro 9.1, OriginLab Corporation, Northampton, Massachusetts, USA, given as

Freundlich model (FM)[59]

$$Q_e = K_F C_e^{1/n} \tag{2}$$

Langmuir model (LM)[60]

$$Q_e = \frac{Q_{max_L} K_L C_e}{1 + K_L C_e} \tag{3}$$

Langmuir−Freundlich model (LFM)[61]

$$Q_e = \frac{K_{LF} C_e^{n_{LF}}}{1 + (Q_{max_{LF}} C_e)^{n_{LF}}} \tag{4}$$

PFOM[62]

$$Q_t = Q_e(1 - e^{-k_1 t}) \tag{5}$$

PSOM[63]

$$Q_t = \frac{k_2 Q_e^2 t}{1 + k_2 Q_e t} \tag{6}$$

Mixed-1,2-order model (MOM)[64]

$$Q_t = Q_e\left(\frac{1 - e^{-k_{1,2}t}}{1 - \eta e^{-k_{1,2}t}}\right) \tag{7}$$

Van't Hoff model[58]

$$\ln K_L = \frac{\Delta S^\circ}{R} - \frac{\Delta H^\circ}{RT} \tag{8}$$

K_F, n, K_L, Q_{max_L}, Q_t, k_1, k_2, ΔS°, ΔH°, R, T, $Q_{max_{LF}}$, n_{LF}, K_{LF}, $k_{1,2}$, and η are the Freundlich constant (mg g^{-1})(L mg^{-1})$^{1/n}$, an empirical constant that represents the adsorption affinity, Langmuir adsorption constant (L mg^{-1}), Q_e for a complete monolayer (mg g^{-1}), amounts of adsorbate ions adsorbed at time t (min) by AFZ (mg g^{-1}), pseudo-first-order rate constant (min^{-1}), pseudo-second-order rate constant (g mg^{-1} min^{-1}), entropy change (J mol^{-1} K^{-1}), enthalpy change (J mol^{-1}), universal gas constant (8.314 J mol^{-1} K^{-1}), absolute temperature (K), Langmuir−Freundlich equilibrium adsorption capacity (mg g^{-1}), Langmuir−Freundlich constant for adsorption affinity, Langmuir−Freundlich constant (mg g^{-1})(L mg^{-1})$^{1/n}$, mixed-1,2-order rate constant (min^{-1}), and mixed-1,2-order exponent (min^{-1}), respectively.

2.4. Characterization of Surface Textural Properties of AFZ. Attenuated total reflectance-infrared (ATR-IR) spectrophotometry was studied by a PerkinElmer Spectrum 100 ATR-IR spectrometer with a Specac Golden Gate ATR unit. The background was obtained by KBr, and the scanning wavenumber range was 400 to 4000 cm^{-1}. Raman spectroscopy was done by using a LabRAM HR Raman micro-

spectrometer (Horiba Scientific, France) with an integrated Olympus BXFM microscope. The measurements were performed with a diode laser (785 nm, max 61 mW at the sample), He−Ne laser (633 nm, max 13.9 mW at the sample), and frequency-doubled neodymium-doped yttrium aluminum garnet (Nd:YAG) laser (532 nm, max 27 mW at the sample). The scanning Raman shift was 100 to 2000 cm^{-1}. Scanning electron microscopy−energy-dispersive X-ray spectroscopy (SEM-EDX) was performed with a SIGMA VP 300 (Carl Zeiss AG, Germany) microscope. Images and spectra were recorded with the In-Lens detector at an acceleration voltage of 1.00−2.00 kV and a working distance between 2.8 and 3.1 mm. Thermogravimetric analysis (TGA) and differential thermogravimetry (DTG) were studied by a NETZSCH STA 449F3 Jupiter. The Al$_2$O$_3$ crucible was used for these analyses with a heating rate of 10 °C min^{-1} from ambient temperature to 1000 °C. X-ray diffraction (XRD) was studied by a Bruker D8 Bragg−Brentano Geometry, with λ: Cu Kα radiation (λ = 0.154 nm) at 40 kV and 40 mA. Samples were ground in isopropanol and dried in a vacuum compartment drier at 40 °C before the measurement. The N$_2$ adsorption/desorption physisorptometry was studied by a Microtrack Belsorp Mini 2 physisorptometer. Samples were degassed at 10 Pa and 200 °C for 3 h before measurements were done. The Brunauer−Emmett−Teller (BET) and T-plot multipoint techniques were used to analyze the surface areas and pore diameters and pore volumes of samples. Also, the solid-state cross-polarization magic angle spinning ^{13}C nuclear magnetic resonance (CP-MAS ^{13}C NMR), Bruker Avance 300 model, equipped with a 9.4 T wide-bore superconducting magnet, a frequency of 300 MHz, and Dispersion Technology Model DT 1200 Zetasizer were used to characterize AFZ. The spectra from X-ray photoelectron spectroscopy (XPS) were obtained in hybrid lens mode at a pass energy of 10 eV and a takeoff angle of 0° with a Kratos Axis Supra setup equipped with a monochromatic Al Kα X-ray source ($h\nu$ = 1486.7 eV) operated with an emission current of 15 mA and an applied power of 225 W. The beam area was set to ≈2 × 1 mm^2 using the slot collimation mode.

3.0. RESULTS AND DISCUSSION

3.1. Characterization of AFZ. *3.1.1. Zeta Potential (ZP).* The zeta potential (ZP) of AFZ at pH 7.3 is +10.8 mV (Figure S1). The implication of this is that the surface of AFZ is highly protonated at pH < PZC and these protons decrease drastically as pH > PZC. It was observed that the uptake of PSMMs by AFZ increased from pH values of 1.0 to 7.0 until a sharp fall was observed at pH > 7.0.[57,58,65] The plausible reason for the protonation of the surface of AFZ at pH ≤ 7.3 and the possession of a positive zeta potential is the modification of coffee waste (a starting material for AFZ synthesis) with concentrated phosphoric acid. Moreover, at pH > PZC, the solution possessed greater negative charges that improved the uptake of PSMMs by AFZ.[65−67] A positive zeta potential shows an increase in the hydrophobic interaction between the target contaminant and adsorbent. In this case, the positive zeta potential increased the hydrophobic interaction between PSMMs and AFZ through π−π interactions, van der Waal interactions, and hydrogen bonding.[68]

3.1.2. Thermogravimetric Analysis (TGA) and Differential Thermogravimetry (DTG). The thermal behavior and stability of materials are best understood with TGA and DTG. The

thermal stability of adsorbents during applications at elevated temperatures is fundamental to their efficiencies.[58,69,70]

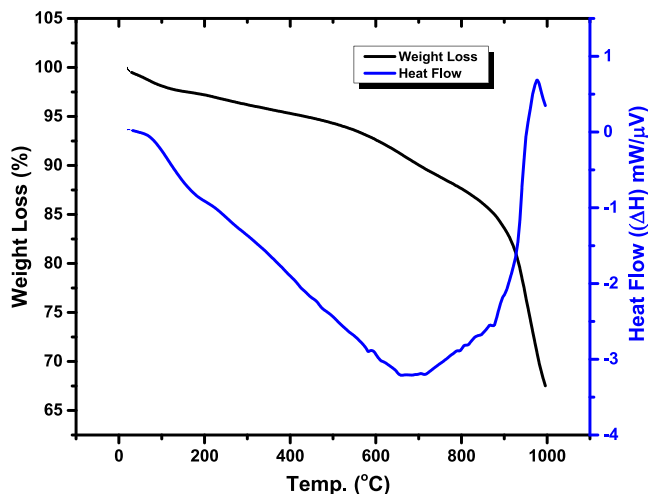Figure 1 shows the TGA and DTG thermograms of AFZ. The TGA thermogram of AFZ has three regions of weight loss.

Figure 1. TGA and DTG thermograms of AFZ.

The first region has 2% weight loss at <200 °C, which was attributable to the loss of moisture.[58,69] The second region has 10% weight loss above 200 to 800 °C, which was due to the loss of solvents, volatile components of the polysaccharides such as galactomannans and arabinogalactans in the coffee waste.[58,71] At this stage, the fragmentation of high molecular weight compounds into small molecules took place. Also, the volatilization of hemicelluloses, cellulose, and lignin took place before the release of various volatile components.[29,58,71] The third region has 20% weight loss above 800 °C due to the carbonization and endothermic thermal decomposition of lignin and cellulose in the coffee waste.[29,58,71]

The DTG thermogram shows (Figure 1) an exothermic shoulder at <700 °C due to the pyrolysis and thermal decomposition of hemicelluloses, cellulose, and lignin.[71,72] An endothermic peak was observed >700 to 960 °C, which was attributed to the formation of some hydrocarbons, carbon dioxide, and carbon monoxide from the pyrolysis of molecular bonds of hemicelluloses, cellulose, and lignin and the condensation of volatiles.[71,72] Above 960 °C, an exothermic peak was observed due to the slow thermal decomposition of lignin into a carbon skeleton.[71,72]

3.1.3. Solid-State Cross-Polarization Magic Angle Spinning ^{13}C Nuclear Magnetic Resonance (CP-MAS ^{13}C NMR). This spectroscopic technique is used to validate the carbon structure of materials with respect to their possible interaction with other atoms. A prominent peak at a chemical shift (δ) of 128 ppm in the spectrum of CP-MAS ^{13}C NMR of AFZ shows the presence of unsaturated carbon signals[73] (Figure S2), which comprise broken glycosidic bonds,[74] aromatic carbons from biochar derived from lignocelluloses,[73,75] and delocalized graphitic planes of carbon formed from the pyrolysis of lignocelluloses, resulting from the carbonization of the hydrophilic matrix of polysaccharides.[75,76] It is evident in this technique that the carbon skeleton in AFZ was formed from the components of various polysaccharides that are found in AFZ.[74,76] These delocalized graphitic planes of the carbon

network in AFZ were responsible for its hydrophobic interaction with PSMMs.

3.1.4. Attenuated Total Reflectance-Infrared (ATR-IR) Spectrophotometry. Figure 2 depicts the ATR-IR spectrum
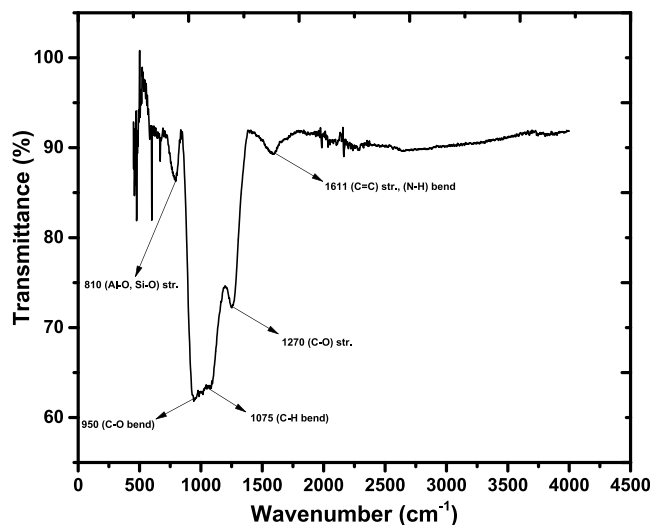

Figure 2. ATR-IR spectrum of AFZ.

of AFZ, which possesses various shoulders at 810, 950, 1075, 1270, and 1611 cm^{-1} corresponding to the Al−O stretch vibration from the zeolite series[68] and symmetric stretch vibration of a siloxane group (due to the Si content of the zeolite series),[68,77] −C−O bend vibration from the carbon skeleton,[68,77] −C−H bend vibration from aromatic carbon and siloxane stretch vibration,[1,68,77,78] −C−O stretch of aromatic carbon and −C=C− stretch vibration from sp^2 carbon, and then, N−H bend of primary amine, respectively.[68,77,78]

3.1.5. Raman Spectroscopy. Figure 3 shows the Raman spectrum of coffee waste biochar. The G-band was observed at 1583 cm^{-1}, which is attributed to graphitic carbon crystallites for the high-frequency phonons of doubly degenerate E_{2g} carbon symmetry at the Brillouin-zone center (BZC).[75,79] The D-band was observed at a Raman frequency of 1351 cm^{-1}, which is attributed to the activation of structural defect
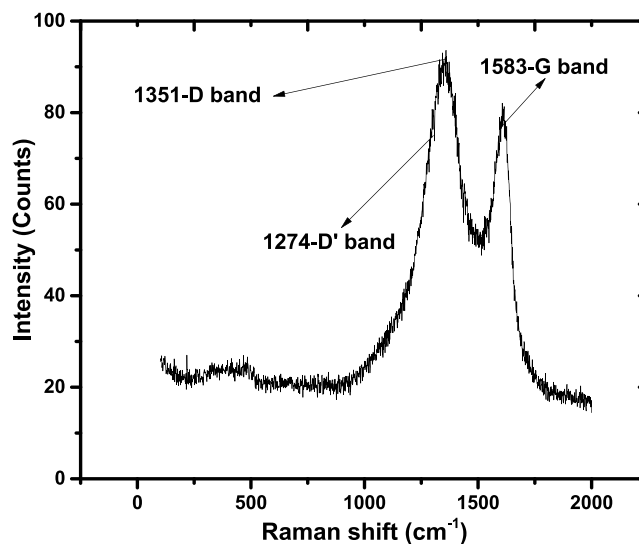

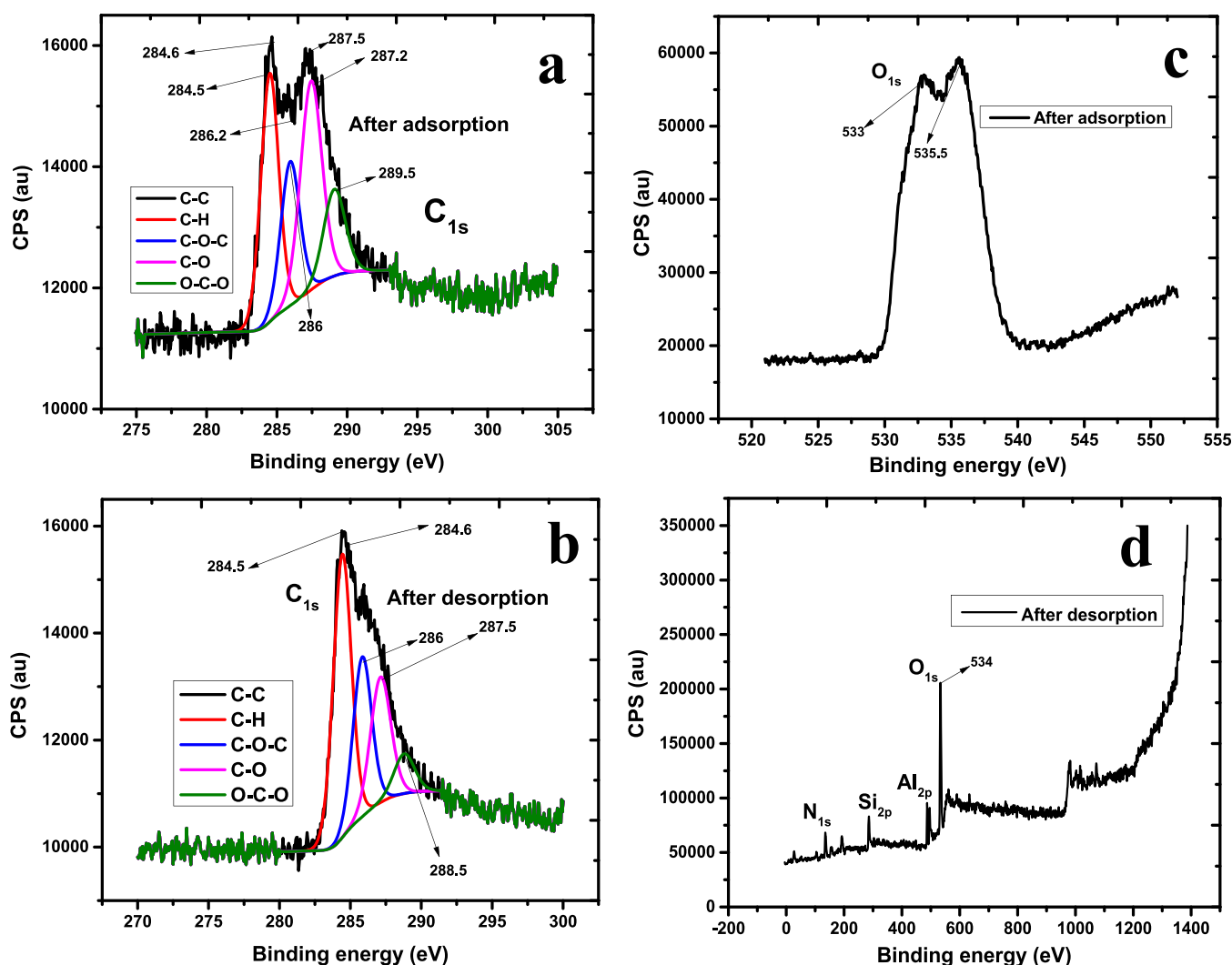**Figure 3.** Raman spectrum of coffee waste biochar.

Figure 4. XPS for C 1s excitation states of (a) AFZ after adsorption of PSMMs and (b) AFZ after desorption of PSMMs and O 1s excitation states of (c) AFZ after adsorption of PSMMs and (d) AFZ after desorption of PSMMs.

resulting from A_{1g} mode breathing vibrations of aromatic sp^2 carbon rings, reflecting a disordered graphitic structure and dislocated crystal phonons arising from alterations in the graphite lattice of the coffee waste biochar.[80] The D'-band was observed at a Raman frequency of 1274 cm^{-1}, which is attributed to the sp^3 phases of disordered graphite lattice in the grain boundaries for the E_{2g} carbon symmetry at the BZC.[81] The crystallite size was calculated by the formula

$$L_a(nm) = \frac{2.4 \times 10^{-10}\lambda^4}{(I_D/I_G)} \qquad (9)$$

where L_a, λ, I_D, and I_G are the crystallite size, wavelength of the laser source (532 nm), ratio of the peak for the D-band, and ratio of the peak for the G-band, respectively. The size of the crystallite is 13.88 nm.[82]

3.1.6. X-ray Photoelectron Spectroscopy (XPS). XPS gives information on the various electronic states of the functional moieties that are involved in the bond formation and chemical interactions between the surfaces of adsorbents and the target molecules (adsorbates).[75,83] The binding energies involved in the interaction(s) between adsorbents and adsorbates are a function of specific delocalized electrons on the surfaces of adsorbents available for chemical interactions with target

contaminant molecules.[84] Figures 4a,b reveal the C 1s excitation states of AFZ after its adsorption and desorption of PSMMs, respectively. From Figures 4a, the C 1s excitation state shows that AFZ comprises C−H, C−O, C−C, C−O−C, and O−C−O bonds, which were found at binding energies of 284.5, 287.2, 284.6, 286, and 289.5 eV, respectively, after adsorption of PSMMs onto its surface. From Figure 4b, after desorption of PSMMs from the surface of AFZ, the binding energies were unaltered for C−H, C−C, and C−O−C bonds. Interestingly, the binding energies were altered for C−O and O−C−O bonds, which showed a slight increase from 287.2 to 287.5 eV with a decrease in peak intensity and a decrease from 289.5 to 288.5 eV with an increase in peak intensity, respectively. The reason for these changes is the fact that the adsorption of PSMMs onto the surface of AFZ led to the formation of weak hydrophobic interactions such as hydrogen bonding, covalent bonding, non covalent aromatic π-system, electron donor−acceptor interactions, van der Waals forces, *etc.*[84,85] This confirms the presence of sp^2 hybridized carbon and carbon skeleton in the AFZ structure that appeared in the form of various bonds in the ATR-IR result in Figure 2.[75] Desorption study showed that only some bonds were affected and altered. Also, Figure 4c reveals that after the adsorption of

PSMMs by AFZ, the O 1s excitation state had two broad peaks at 533 and 535.5 eV that were involved in the formation of N−H, Si−O, and Al−O bonds, as shown in Figure 2.[85,86] For Figure 4d, N 1s, Si 2p, and Al 2p excitation states for AFZ appeared at 135, 289, and 488.5 eV, respectively, in addition to O 1s that appeared at 534 eV after the desorption of PSMMs from its surface. This confirms the presence of N−H, Si−O, and Al−O functional groups on the surface of AFZ, as shown in Figure 2.

3.1.7. X-ray diffraction (XRD). Figure 5 shows the XRD patterns of AFZ after the adsorption and desorption of
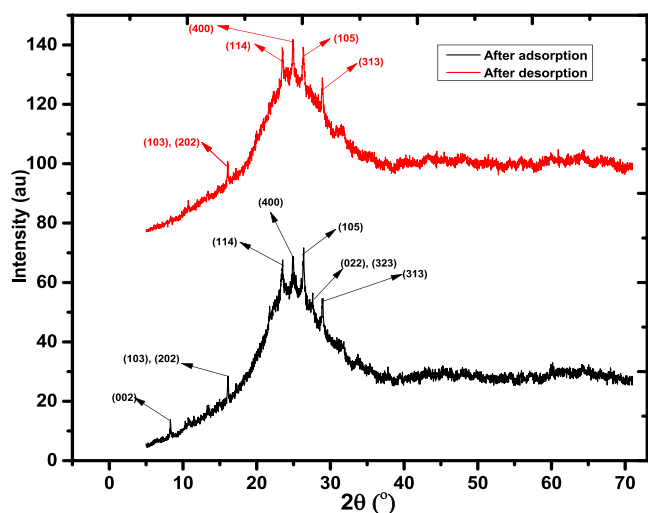

Figure 5. XRD patterns of AFZ after adsorption and desorption.

PSMMs. The Miller indices of AFZ after adsorption of PSMMs appeared at 8.5, 15.7, 23.5, 25, 26.5, 27.5, and 29°, which revealed that these phases correspond to the (002), (103) + (202), (114), (400), (105), (022) + (323), and (313) diffraction planes, respectively, that are attributed to the presence of silica and alumina constituents in the zeolite series that are crystalline[73,76,87] and the presence of amorphous graphitic carbon symmetry[73,76] (card no.: PDF 89-1397). It is interesting to note that the constituent of biochar in AFZ is responsible for the amorphous phases that are found between 15.7 and 35°, which reveals stacking reflection of conjugated aromatic carbon, unraveling a graphitic structure.[68] These broad amorphous phases in AFZ are an indication of the large presence of graphitic carbon matrix over the zeolite phase. After desorption of PSMMs, it was observed that the Miller indices of the diffraction peaks of AFZ at 8.5 and 27.5° disappeared. Also, there was a shift in the diffraction peak that appeared at 15.7° (after adsorption) to 17° (after desorption). These changes that resulted from a shift and disappearance of diffraction peaks after desorption might likely be due to the disentanglement of covalent bonds and noncovalent aromatic π-bonds.[87,88] Other diffraction peaks of AFZ at 23.5, 25, 26.5, and 29° were unchanged after desorption of PSMMs. This implies that after desorption, the surface of AFZ was not deformed of the mixed phases of silica and alumina.[88] The crystallite size was calculated using $n\lambda = 2d \sin \theta$ (eq 10), where $n = 1$ and λ, d, and θ are the wavelength of X-rays, d-spacing, and Bragg's angle, respectively. The crystallite sizes for AFZ after the adsorption of PSMMs were 0.077 ($2\theta = 15.7°$), 0.121 ($2\theta = 26.5°$), 0.083 ($2\theta = 27.5°$), and 0.082 nm ($2\theta = 29°$) for the (103) + (202), (105), (022) + (323), and (313)

diffraction planes, respectively. These crystallite sizes were unchanged after the desorption of PSMMs from AFZ.[82]

3.1.8. Scanning Electron Microscopy (SEM). Figures 6a−c and 6d−f show the SEM images of the surfaces of AFZ before and after adsorption of PSMMs, respectively. The surface of AFZ before the adsorption of PSMMs comprises large lumps of clogged and agglomerated particles that appeared to contain a distribution of small and large pores. After the adsorption of PSMMs onto AFZ, its surface appeared to be coarse, and the small and large pores disappeared. This coarseness and disappearance of small and large pores suggest the presence of PSMMs on the surface of AFZ. Figures 6g,h show the EDX spectra of AFZ before and after adsorption of PSMMs, respectively. From these EDX spectra, it was observed that the peak intensities of C and O for AFZ after the adsorption of PSMMs were greater than those of AFZ before the adsorption of PSMMs. This accounts for the adsorbed PSMMs on the surface of AFZ.[57,58,69,75,78] Table 1 reveals the elemental (CHNS) composition of the coffee waste, supporting the fact that the coffee waste consists of different atomic constituents.

3.1.9. Brunauer−Emmett−Teller (BET) Physisorptometry. Figure 7a−d shows the plots of N_2 gas uptake (cm^3 g^{-1} STP) against relative pressure and N_2 gas uptake (cm^3 g^{-1} STP) and

$$\frac{1}{\left[W\left(\left(\frac{P_0}{P} \right) - 1 \right) \right]}$$ against relative pressure before and after adsorption.

The BET specific surface area and pore volume of AFZ before and after adsorption of PSMMs were 79 m^2 g^{-1} and 0.09 cm^3 g^{-1} and then 33 m^2 g^{-1} and 0.08 cm^3 g^{-1}, respectively. These plots show that the pores of AFZ were readily available for the uptake of PSMMs, in addition to its active sites. The BET specific surface area and pore volume of AFZ decreased after the adsorption of PSMMs,[58,75] which is an indication that the adsorbed PSMMs occupied the active sites and pores on the surface of AFZ after adsorption. During the adsorption process, the surface and pores of AFZ play significant roles as follows:

First is the diffusion of adsorbate (PSMMs) through the solution to the external surface of the adsorbent (AFZ) or the boundary layer diffusion of the adsorbate or solute molecules (surface or boundary layer diffusion); second is the gradual adsorption, in which intraparticle diffusion may be a rate-limiting step (intraparticle diffusion); third is the diffusion of adsorbate particles to adsorption sites either by pore diffusion through the liquid-filled pores or by a solid diffusion mechanism (pore diffusion or solid diffusion). Some of the adsorbates are adsorbed onto the adsorbent by a combination of one, two, or three diffusion mechanisms.[57,89−91] Also, the activation and pyrolysis of biomasses have been understood to cause the formation of irregular carbon layers that comprised abundant small-sized pores, which played a vital role in the adsorption of target contaminants.[75,92,93] Noteworthy of mention is that numerous published papers focused and dwelt on adsorbents with a large surface area and pore size as the only platform in which more functional moieties (active sites) and pore channels could be made available for enhanced adsorption processes. Generally, it is understood that the small surface area and pore size of adsorbents prevent target contaminant molecules from accessing more active sites and pore channels during adsorption processes. As reasonable as these claims are, it is pertinent to understand that only the formation of an appropriate surface area and pore size can
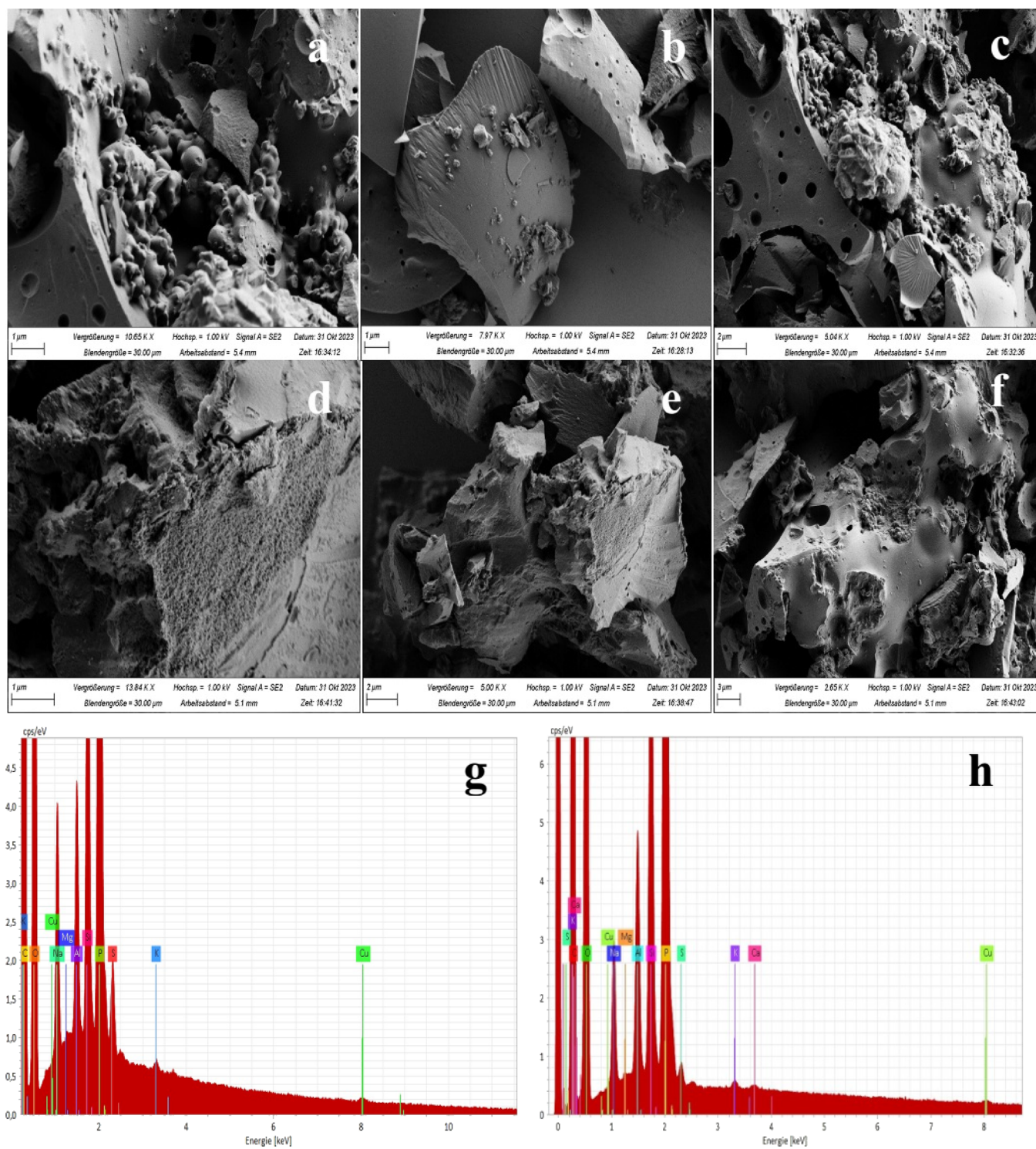
Figure 6. (a−c) SEM images for AFZ, (d−f) SEM images for PSMMs adsorbed on AFZ, (g) EDX spectrum for AFZ, and (h) EDX spectrum for PSMMs adsorbed on AFZ.

Table 1. CHNS Elemental Analysis of Coffee Waste

elements	C	H	N	S	O
% relative abundance	67.60	4.94	0.75	0.86	25.85

enhance adsorption of target contaminant molecules. The appropriate surface area and pore size mean a large surface area and pore size, coupled with readiness to adsorb or trap target contaminant molecules through an intragranular diffusion mechanism. Intragranular diffusion rapidly enhances the entrapment of adsorbates onto adsorbents (adsorbate–adsorbent interactions) by weak hydrophobic interactions such as hydrogen bonding, covalent bonding, noncovalent aromatic π-system, electron donor–acceptor interactions, van der Waals forces, *etc.*[94−98]

3.2. Adsorption Studies. *3.2.1. Effect of pH on the Adsorption of PSMMs.* The solution pH is an essential experimental factor influencing the adsorption of PSMMs by
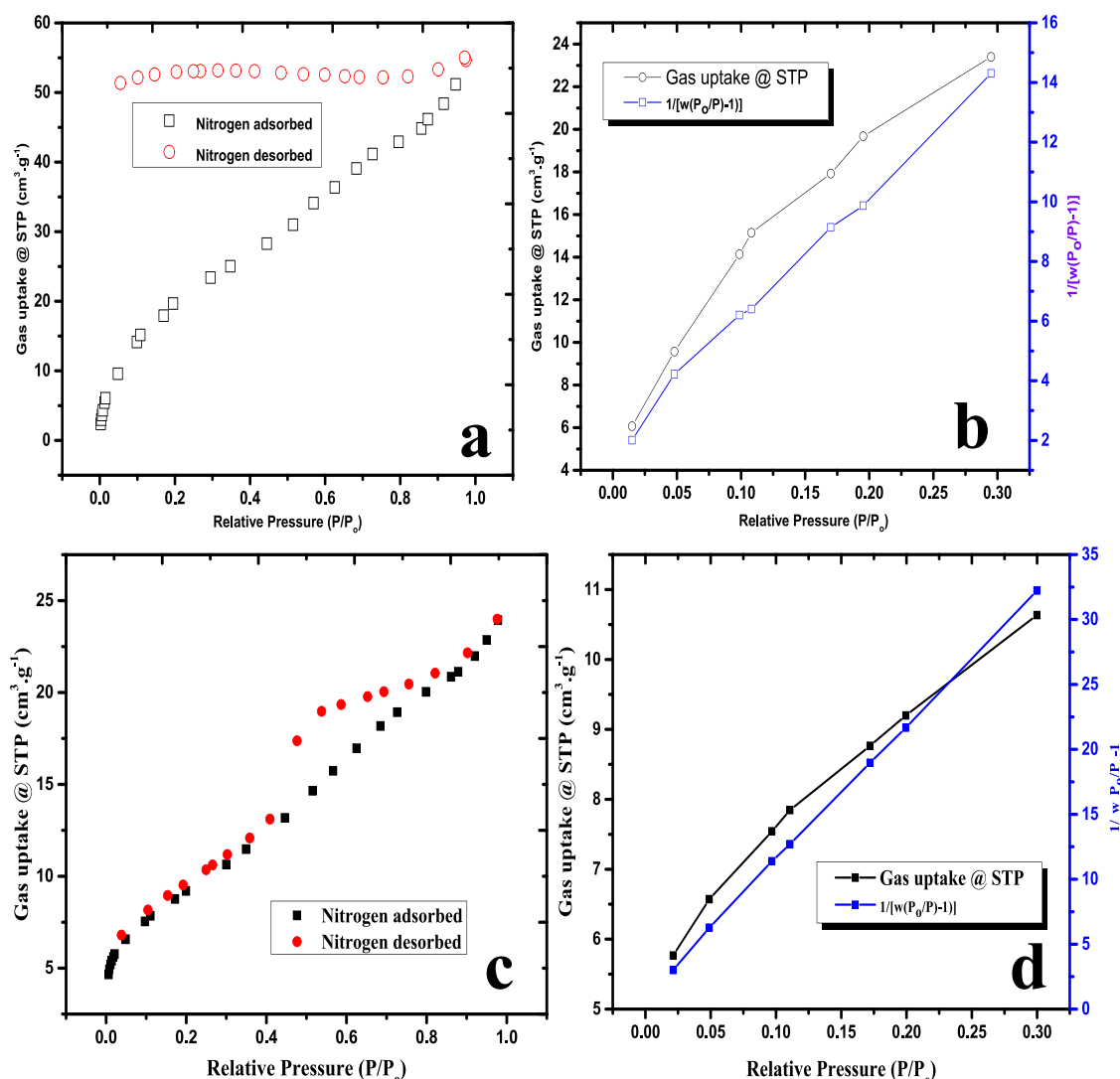
Figure 7. Plots of (a) N_2 gas uptake (cm^3 g^{-1} STP) against relative pressure before adsorption, (b) N_2 gas uptake (cm^3 g^{-1} STP) and ($\frac{1}{\left[W\left(\left(\frac{P_o}{P}\right)-1\right)\right]}$) against relative pressure before adsorption, (c) N_2 gas uptake (cm^3 g^{-1} STP) against relative pressure after adsorption, and (d) N_2 gas uptake (cm^3 g^{-1} STP) and ($\frac{1}{\left[W\left(\left(\frac{P_o}{P}\right)-1\right)\right]}$) against relative pressure after adsorption.

AFZ.[99] From the pH studies, it was observed that the amount (Q_e) of PSMMs adsorbed by 0.05 g of AFZ increased from 3.94 to 4.70 mg g^{-1} (79 to 94%) from pH values of 1.0 to 7.0, respectively. However, there was a decrease in the amount of PSMMs adsorbed by AFZ from 4.70 to 4.22 mg g^{-1} (94 to 84.4%) at pH > 7.0 (Figure S3). The implication of this is that the PSMM molecules filled the active sites of AFZ increasingly as its surface became deprotonated, with a reduction in the active sites available on the surface of AFZ. Thereafter, there was decrease in the uptake of PSMMs by AFZ at pH > 7.0.[20,57,58] It is understood that polystyrene particles are negatively charged based on their surfaces, irrespective of the fact that they are not specifically functionalized. This property favored the uptake of PSMMs by AFZ below the ZP of 7.3.[100]

3.2.2. Effect of Adsorbent Dose on the Adsorption of PSMMs. Adsorbent dose is a vital process variable in determining the adsorption capacities of adsorbents as a function of the weight differential. It was observed that as the mass of AFZ increased from 0.05 to 1.25 g, the uptake of PSMMs decreased from 4.97 to 0.04 mg g^{-1} (99 to 0.77%),

respectively (Figure S4). This can be explained by agglomeration or aggregation of AFZ with increasing mass, which leads to an increase in its diffusion path of PSMMs during the adsorption process. This phenomenon decreased the rate of diffusion of PSMMs into the film or boundary layer, intraparticles, and pores of AFZ.[58,69] The mass transfer of adsorbates (solutes) onto the surfaces of adsorbents gives information about the diffusion pathway (mass transport) during adsorbate−adsorbent interaction. Mass transfer gives an account of the diffusion of PSMMs from the bulk solution to the AFZ particle surface, diffusion of PSMMs across the boundary layer of AFZ particles, and intraparticle diffusion of PSMMs from the boundary layer into the pore walls of AFZ.[101,102] The mass transfer coefficient was calculated using the mathematical expression, $-\frac{dC}{dt} = K_S S_{BET}(C_t - C_e)$ (eq 11).

As time $t = 0$, $C_e = 0$, eq 11 becomes $\left|\frac{d(C_t/C_o)}{dt}\right|_{t=0} = -K_S S_{BET}$.

The terms C_t, K_S, and S_{BET} are adsorbate concentrations at t (min), mass transfer coefficient (m s^{-1}), and BET surface area
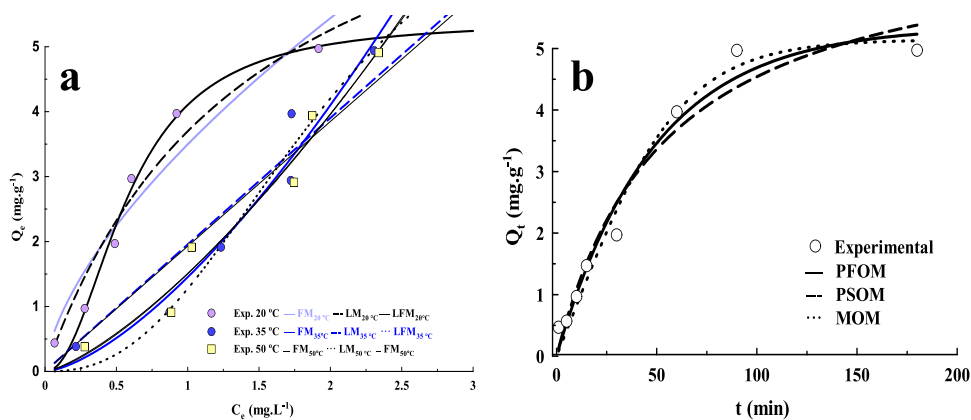
Figure 8. (a) Plot of Q_e (mg g^{-1}) against C_e (mg·L^{-1}) for the adsorption of PSMMs by AFZ at different temperatures (adsorbent dose: 0.05 g, agitation time: 180 min, temperature: 20 °C, initial concentration: 1−10 mg·L^{-1}, pH: 7.0); (b) plot of Q_t (mg g^{-1}) against t (min) (adsorbent dose: 0.05 g, agitation time: 1−180 min, temperature: 20 °C, initial concentration: 10 mg·L^{-1}, pH: 7.0).

(m^2 g^{-1}), respectively. The mass transfer coefficient was 1.73×10^{-6} m.s^{-1}. This implies that the K_S value is the diffusion rate of the molecules of PSMMs onto the particle surface and pore walls of AFZ, which is required to break the mass transfer resistance barrier for adsorption to occur.[102,103]

3.2.3. Adsorption Equilibrium. Adsorption equilibrium explores the mathematical relationship between the equilibrium concentration of known contaminant solutes (adsorbates) and solid materials (adsorbents) at a particular temperature.[58,104] Also, it is a solid−liquid/fluid interphase, in which the adsorbates are concentrated on the surfaces of the adsorbents.[104] For this study, the adsorption of PSMMs by AFZ increased from 0.44 to 4.97 mg g^{-1} (8.80 to 99.4%), 0.38 to 4.94 mg g^{-1} (7.60 to 98.8%), and 0.38 to 4.91 mg g^{-1} (7.60 to 98.2%) at 20, 35, and 50 °C at an adsorbent dosage of 0.05 g, respectively. This trend is attributable to the increase in temperature from 20 to 50 °C, which led to rapid mobility of the PSMMs molecules onto the surface of AFZ, respectively. The rise in temperature led to the increase in the kinetic energy of the PSMM molecules as they migrate to the surface of AFZ.[57,69]

The adsorption equilibrium studies have shown that the nonlinear LFM best fits the experimental data (Figure 8a), with correlation coefficients (R^2) of 0.99 in all cases and the adsorption capacity, $Q_{e_{LF}}$, from 4.78 to 4.85 mg g^{-1} at 20 to 50 °C, with SSE values from 0.21 to 0.17, respectively (Table 2). This shows that the surface of AFZ comprises both homogeneous and heterogeneous layers. Therefore, the uptake of PSMMs by AFZ was a combination of chemisorption and physisorption. It occurred that the molecules of PSMMs filled the single-existing active sites of AFZ first before filling its combined active sites.[19,20]

The partition coefficients, K_D (a linear adsorption constant (L g^{-1})), are recognized as Henry's isotherm, which is analyzed and indexed as the linear relationship between the adsorbed solute and the quantity of bulk solute in the solution at equilibrium. The partition coefficient, K_D, is given as $Q_e = K_D C_e$ (eq 12).[35,105] The K_D values for the adsorption of PSMMs by AFZ are 1.52 to 3.86, 4.35 to 9.55, and 4.75 to 9.69 L g^{-1} for 20, 35, and 50 °C, respectively. The K_D values for the adsorption of PSMMs by AFZ increased with rise in temperature, which implies that electrostatic interactions, van der Waals interactions, and hydrophobic interactions played an active role in the adsorption process.[105]

Table 2. Isotherm Parameters at Different Temperatures for the Adsorption of PSMMs by AFZ

Temperatures	20 °C	35 °C	50 °C
Isotherm Models			
FM			
$1/n$	0.805	0.059	0.046
K_F(mg.g^{-1})(L.mg^{-1})$^{1/n}$	1.568	0.668	0.710
r^2	0.962	0.977	0.983
SSE	0.285	0.181	0.125
LM			
Q_{max_L}(mg.g^{-1})	4.54	4.58	4.63
K_L(L.mg^{-1})	0.069	0.031	0.022
r^2	0.987	0.988	0.989
SSE	0.166	0.400	0.291
LFM			
$Q_{max_{LF}}$(mg.g^{-1})	4.78	4.82	4.85
K_{LF}(mg.g^{-1})(L.mg^{-1})$^{1/n}$	0.050	0.070	0.090
n_{LF}	0.001	0.004	0.007
r^2	0.999	0.999	0.999
SSE	0.212	0.183	0.166

3.2.4. Adsorption Kinetics and Thermodynamics. Adsorption kinetics is concerned with the mass transfer rate of adsorbates or solute ions onto the surfaces of adsorbents.[69] This process facilitates the migration of solute ions from bulk solutions into the active sites of adsorbents.[69] This process is achieved by the steady diffusion of adsorbates from the bulk solutions into the boundary or film layers of adsorbents and the steady diffusion of adsorbates from the boundary or film layers of adsorbents into their intraparticles and pores.[57,58,69] This study revealed that 0.47 to 4.97 mg g^{-1} PSMMs were adsorbed by AFZ for an agitation time of 1 to 180 min, respectively. The kinetics studies have shown that the MOM best fit the experimental data (Figure 8b), with the value of Q_e of 4.90 mg g^{-1}, a correlation coefficient (R^2) of 1.00, and an SSE value of 0.02 (Table 3). The PSMM molecules were rapidly adsorbed by AFZ from 1 to 90 min. After 90 min, the surface of AFZ was saturated, resulting in further uptake of PSMM molecules by AFZ. Table 4 shows the thermodynamic parameters for the uptake of PSMM molecules by AFZ. The adsorption process at all temperatures were nonspontaneous ($\Delta G°$ was positive at all temperatures). Also, the adsorption

Table 3. Kinetic Parameters for the Adsorption of PSMMs by AFZ

Kinetic Models	Parameter Values
PFOM	
$Q_e (mg\ g^{-1})$	4.361
$k_1 (min^{-1})$	0.021
r^2	0.987
SSE	0.214
PSOM	
$Q_e (mg\ g^{-1})$	4.653
$k_2 (g\ mg^{-1}\ min^{-1})$	0.013
r^2	0.991
SSE	0.171
MOM	
$Q_e (mg\ g^{-1})$	4.898
$k_{1,2}\ (g\ mg^{-1}\ min^{-1})$	0.007
η	0.036
r^2	1.000
SSE	0.014

Table 4. Thermodynamic Parameters for the Adsorption of PSMMs by AFZ

	20 °C	35 °C	50 °C
$\Delta G° (kJ\ mol^{-1})$	+66.9	+68.8	+70.7
$\Delta H° (kJ\ mol^{-1})$	+30.2		
$\Delta S° (J\ mol^{-1}.K^{-1})$	−126		

process was endothermic, with a decrease in the degree of entropy at which adsorption occurred.[57]

3.2.5. Plausible Adsorption Mechanism for the Uptake of PSMMs onto AFZ. The adsorption mechanism of the adsorption processes provides an understanding of the chemical interaction between adsorbates and adsorbents. Also, the adsorption mechanism gives useful information on the process dynamics of the uptake of target contaminants

onto the surfaces of adsorbents.[75] The characterization of the surface of AFZ by ATR-IR, XPS, and CHNS analyses revealed that it comprises various functional groups, which are C−H, C−O, C=C, N−H, Al−O, and Si−O. These moieties were responsible for hydrophobic interactions between the π-electrons of the sp² orbital of the carbon in AFZ and the π-electrons of the PSMM molecules, π−π aromatic interactions between AFZ and the molecules of PSMMs, electrostatic attraction between the molecules of slight negatively charged PSMMs and AFZ, hydrogen bonding between AFZ and the molecules of PSMMs, electron donor−acceptor interactions, and weak van der Waals forces.[43,98] Also, the chemical interaction between PSMMs by AFZ was a combination of chemisorption and physisorption mechanisms, which involves the rapid filling of the active sites on the surface of AFZ with PSMMs to form a monolayer that in turn became active sites for other molecules of PSMMs to form a multilayer on the surface of AFZ.[61,95,98]

3.2.6. Recycle Study. Recycle study is vital for the continuous usage, sustainability, eco-friendliness, and cost reduction of producing adsorbents.[21] The recycle study for PSMM-loaded AFZ was done six times, as shown in Figure 9. This study reveals that AFZ achieved 92.2−68.0% removal of PSMMs in deionized water (DW) from the first to sixth cycles. Also, it was observed that 1.0 M HNO₃, acetone, and ethanol from the first to sixth cycles achieved 72.7−53.0, 63.0−36.0, and 17.6−9.0%, respectively. This implies that AFZ has good recovery potential for the removal of PSMMs in DW. The removal ability of most of the solvents is significantly small, probably due to the fact that PSMMs are held onto the surface of AFZ by chemisorption through electrostatic attraction, π−π aromatic stacking, and other hydrophobic interactions. Table 5 shows the adsorption capacities of different materials for PSMMs compared to AFZ.

3.3. Adsorption of PSMMs from Real Life Water Samples. Above the laboratory applications of AFZ to
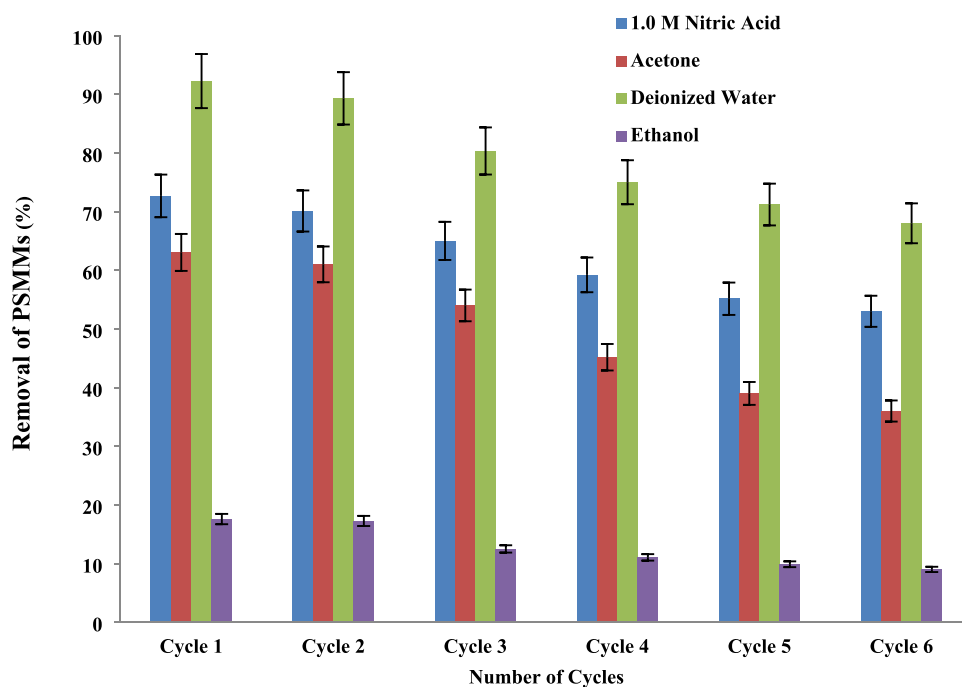

Figure 9. Recycle study of PSMM-loaded AFZ over six cycles (adsorbent dose: 0.05 g; agitation time: 180 min; temperature: 20 °C; pH: 7.0).

Table 5. Comparison of Adsorption Capacities of Some Adsorbents for the Removal of PSMMs[a]

S/No.	Adsorbents	Q_{max} (mg·g^{-1})	Conditions	ref.
1	Mg/Zn modified biochar	374.57	pH = —, T = 25 °C, IC = 300 mg·L^{-1}, AD = 100 mg	17
2	Chitin sponge materials	5.44	pH = 7.0, T = 25 °C, IC = 20 mg·L^{-1}, AD = 10 mg	18
3	Graphene/layer double oxide	209.39	pH = 9.0, T = 25 °C, IC = 400 mg·L^{-1}, AD = 250 mg	19
4	Magnetic ZIF-8	24.50	pH = —, T = 25 °C, IC = 25 mg·L^{-1}, AD = 5 mg	20
5	Fly ash magnetic material	89.90	pH = 7.0, T = 25 °C, IC = 30 mg·L^{-1}, AD = 20 mg	21
6	Chitin/graphene oxide sponge	5.90	pH = 6.0, T = 25 °C, IC = 15 mg·L^{-1}, AD = 10 mg	25
7	Aquifer fine sand	0.00857	pH = 7.0, T = 25 °C, IC = 10 mg·L^{-1}, AD = 2 g	26
8	Reduced graphene oxide	617.28	pH = 6.0, T = 26 °C, IC = 600 mg·L^{-1}, AD = 1.5 mg	28
9	Magnetic iron oxide	2,799.20	pH = 3.0, T = 25 °C, IC = 300 mg·L^{-1}, AD = 100 mg	29
10	Cr-MOF	319.49	pH = 5.0, T = 25 °C, IC = 70 mg·L^{-1}, AD = 4 mg	55
11	Co/Mn-Kaolin	22.00	pH = —, T = 25 °C, IC = 100 mg·L^{-1}, AD = 10 mg	106
12	Fe-Kaolin	13.68	pH = —, T = 25 °C, IC = 100 mg·L^{-1}, AD = 10 mg	106
13	Fe_3O_4 nanoparticles	7.9	pH = 6.5, T = 25 °C, IC = 60 mg·L^{-1}, AD = 60 mg	107
14	Sugar cane bagasse biochar	44.9	pH = —, T = 25 °C, IC = 10 mg·L^{-1}, AD = 15 mg	108
15	Granular activated carbon	2.2	pH = 7.4, T = 25 °C, IC = 40 mg·L^{-1}, AD = 5 g	109
16	AFZ	4.85	pH = 7.0, T = 25 °C, IC = 10 mg·L^{-1}, AD = 50 mg	This study

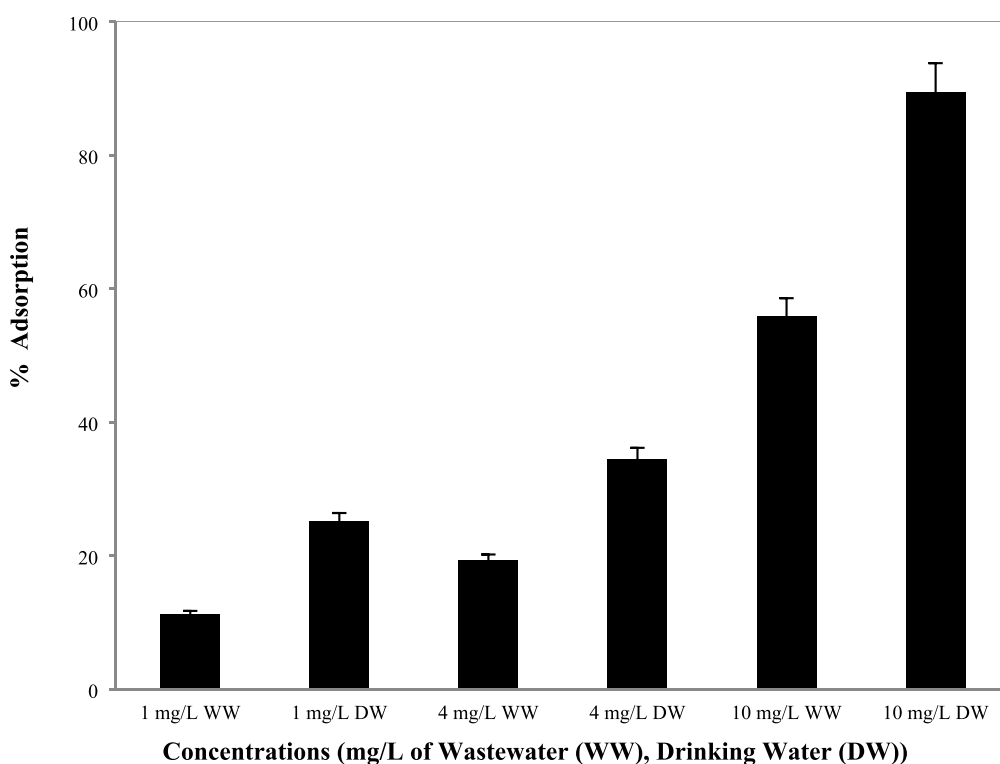[a]Note: IC: Initial concentration, AD: Adsorbent dosage

Figure 10. Percent removal amounts of PSMMs in drinking water and wastewater by AFZ.

cleanup aqueous solutions contaminated with PSMMs, further studies were carried out to understand the potential of AFZ to cleanup real-life water samples. Table S1 shows the physicochemical properties of WW contaminated with PSMMs. The amounts of PSMM molecules removed by AFZ from real life water samples were 11.1 to 55.8% from 1 to 10 mg·L^{-1} for WW and 25.1 to 89.3% from 1 to 10 mg·L^{-1} for DW, respectively (Figure 10). The amounts of PSMM molecules removed by AFZ were higher in DW than WW due to the fact that the WW is a matrix of other contaminants and PSMM molecules, thereby decreasing its adsorption capacity when compared to DW.[28] It should be noted that the tests were carried out with the WWTP inflows since microplastics are found there in particular.

4.0. CONCLUSIONS

Finally, amino-functionalized zeolite series/H_3PO_4-biochar (AFZ) demonstrated potential for the removal of polystyrene monodispersed microsphere suspension (PSMMs) in aqueous solutions, drinking water, and wastewater. The surface characterization of AFZ showed the graphitic matrix, and some functional moieties such as aromatic olefin, amine, hydroxyl, carbonyl, and carboxyl were responsible for the uptake of PSMMs by AFZ. Data analysis revealed that the uptake of PSMMs by AFZ occurred by a combination of chemisorption and physisorption, in which the moieties on the surface of AFZ were responsible for hydrophobic interactions between the π-electrons of the sp^2 orbital of the carbon in AFZ

and the π-electrons of the PSMMs molecules, π–π aromatic interactions between AFZ and the molecules of PSMMs, electrostatic attraction between the molecules of slightly negatively charged PSMMs and AFZ, hydrogen bonding between AFZ and the molecules of PSMMs, electron donor–acceptor interactions, and weak van der Waals forces. AFZ showed potential for the removal of MPs from contaminated water.

■ ASSOCIATED CONTENT

ⓢ Supporting Information

The Supporting Information is available free of charge at https://pubs.acs.org/doi/10.1021/acs.iecr.3c03971.

> Physicochemical characterization of wastewater; list of abbreviations; zeta potential (ZP) of AFZ; CP-MAS ^{13}C NMR spectrum of AFZ; plots of Q_e (mg g^{-1}) against pH for the adsorption of PSMMs by AFZ and Q_e (mg g^{-1}) against adsorbent dosage (g) for the adsorption of PSMMs by AFZ (PDF)

■ AUTHOR INFORMATION

Corresponding Author

Martins O. Omorogie − *Chair of Urban Water Systems Engineering, School of Engineering and Design, Technical University of Munich, Garching 85748, Germany; Department of Chemical Sciences, Faculty of Natural Sciences and Environmental Science and Technology Research Unit, African Centre of Excellence for Water and Environmental Research (ACEWATER), Redeemer's University, Ede 232101, Nigeria;* ⓞ orcid.org/0000-0001-9697-2960; Email: mo.omorogie@tum.de, omorogiem@run.edu.ng, dromorogiemoon@gmail.com

Author

Brigitte Helmreich − *Chair of Urban Water Systems Engineering, School of Engineering and Design, Technical University of Munich, Garching 85748, Germany;* ⓞ orcid.org/0000-0003-4224-3329

Complete contact information is available at:
https://pubs.acs.org/10.1021/acs.iecr.3c03971

Notes

The authors declare no competing financial interest.

■ ACKNOWLEDGMENTS

■ REFERENCES

(1) John, K. I.; Omorogie, M. O.; Bayode, A. A.; Adeleye, A. T.; Helmreich, B. Environmental microplastics and their additives—a critical review on advanced oxidative techniques for their removal. *Chemical Papers* **2023**, *77*, 657–676.

(2) Ali, I.; Tan, X.; Li, J.; Peng, C.; Wan, P.; Naz, I.; Duan, Z.; Ruan, Y. Innovations in the Development of Promising Adsorbents for the Remediation of Microplastics and Nanoplastics−A Critical Review. *Water Res.* **2023**, *230*, No. 119526.

(3) Europe, P. Plastics—the facts 2022. *PlasticEurope* **2022**, *1*, 1−64.

(4) Department, S. R. *Production forecast of thermoplastics worldwide from 2025 to 2050*: United States of America, New York2023.

(5) Aslani, H.; Pashmtab, P.; Shaghaghi, A.; Mohammadpoorasl, A.; Taghipour, H.; Zarei, M. Tendencies towards bottled drinking water consumption: Challenges ahead of polyethylene terephthalate (PET) waste management. *Health Promotion Perspectives* **2021**, *11*, 60.

(6) Cabernard, L.; Pfister, S.; Oberschelp, C.; Hellweg, S. Growing environmental footprint of plastics driven by coal combustion. *Nature Sustainability* **2022**, *5*, 139−148.

(7) Geyer, R.; Jambeck, J. R.; Law, K. L. Production, use, and fate of all plastics ever made. *Sci. Adv.* **2017**, *3*, No. e1700782.

(8) Law, K. L.; Narayan, R. Reducing environmental plastic pollution by designing polymer materials for managed end-of-life. *Nature Reviews Materials* **2022**, *7*, 104−116.

(9) Ali, I.; Tan, X.; Li, J.; Peng, C.; Naz, I.; Duan, Z.; Ruan, Y. Interaction of microplastics and nanoplastics with natural organic matter (NOM) and the impact of NOM on the sorption behavior of anthropogenic contaminants−A critical review. *Journal of Cleaner Production* **2022**, *376*, No. 134314.

(10) Luo, X.; Wang, Z.; Yang, L.; Gao, T.; Zhang, Y. A review of analytical methods and models used in atmospheric microplastic research. *Sci. Total Environ.* **2022**, *828*, No. 154487.

(11) Alimi, O. S.; Farner Budarz, J.; Hernandez, L. M.; Tufenkji, N. Microplastics and nanoplastics in aquatic environments: aggregation, deposition, and enhanced contaminant transport. *Environ. Sci. Technol.* **2018**, *52*, 1704−1724.

(12) Jan Alexander, L. B. A.; Bignami, M.; Ceccatelli, S.; Cottrill, B.; Dinovi, M.; Edler, L.; Grasl-Kraupp, B.; Hogstrand, C.; Hoogenboom, L.; Knutsen, H. K.; Nebbia, C. S.; Oswald, I.; Petersen, A.; Rogiers, V. M.; Rose, M.; Roudot, A.-C.; Schwerdtle, T.; Vleminckx, C.; Vollmer, G.; Wallace, H. Presence of microplastics and nanoplastics in food, with particular focus on seafood. *EFSA J.* **2016**, *14*, No. e04501.

(13) Nizzetto, L.; Langaas, S.; Futter, M. Pollution: do microplastics spill on to farm soils? *Nature* **2016**, *537*, 488−488.

(14) Ragusa, A.; Svelato, A.; Santacroce, C.; Catalano, P.; Notarstefano, V.; Carnevali, O.; Papa, F.; Rongioletti, M. C. A.; Baiocco, F.; Draghi, S. Plasticenta: First evidence of microplastics in human placenta. *Environ. Int.* **2021**, *146*, No. 106274.

(15) Wright, S. L.; Kelly, F. J. Plastic and human health: a micro issue? *Environ. Sci. Technol.* **2017**, *51*, 6634−6647.

(16) Ya, H.; Jiang, B.; Xing, Y.; Zhang, T.; Lv, M.; Wang, X. Recent advances on ecological effects of microplastics on soil environment. *Science of The Total Environment* **2021**, *798*, No. 149338.

(17) Wang, J.; Sun, C.; Huang, Q.-X.; Chi, Y.; Yan, J.-H. Adsorption and thermal degradation of microplastics from aqueous solutions by Mg/Zn modified magnetic biochars. *Journal of hazardous materials* **2021**, *419*, No. 126486.

(18) Sun, C.; Wang, Z.; Zheng, H.; Chen, L.; Li, F. Biodegradable and re-usable sponge materials made from chitin for efficient removal of microplastics. *Journal of Hazardous Materials* **2021**, *420*, No. 126599.

(19) Peng, G.; Xiang, M.; Wang, W.; Su, Z.; Liu, H.; Mao, Y.; Chen, Y.; Zhang, P. Engineering 3D graphene-like carbon-assembled layered double oxide for efficient microplastic removal in a wide pH range. *Journal of Hazardous Materials* **2022**, *433*, No. 128672.

(20) Pasanen, F.; Fuller, R. O.; Maya, F. Fast and simultaneous removal of microplastics and plastic-derived endocrine disruptors using a magnetic ZIF-8 nanocomposite. *Chemical Engineering Journal* **2023**, *455*, No. 140405.

(21) Zhao, H.; Huang, X.; Wang, L.; Zhao, X.; Yan, F.; Yang, Y.; Li, G.; Gao, P.; Ji, P. Removal of polystyrene nanoplastics from aqueous solutions using a novel magnetic material: Adsorbability, mechanism, and reusability. *Chemical Engineering Journal* **2022**, *430*, No. 133122.

(22) Singh, N.; Khandelwal, N.; Ganie, Z. A.; Tiwari, E.; Darbha, G. K. Eco-friendly magnetic biochar: An effective trap for nanoplastics of varying surface functionality and size in the aqueous environment. *Chemical Engineering Journal* **2021**, *418*, No. 129405.

(23) Wang, Z.; Sun, C.; Li, F.; Chen, L. Fatigue resistance, re-usable and biodegradable sponge materials from plant protein with rapid

water adsorption capacity for microplastics removal. *Chemical Engineering Journal* **2021**, *415*, No. 129006.

(24) Tang, Y.; Zhang, S.; Su, Y.; Wu, D.; Zhao, Y.; Xie, B. Removal of microplastics from aqueous solutions by magnetic carbon nanotubes. *Chemical Engineering Journal* **2021**, *406*, No. 126804.

(25) Sun, C.; Wang, Z.; Chen, L.; Li, F. Fabrication of robust and compressive chitin and graphene oxide sponges for removal of microplastics with different functional groups. *Chemical Engineering Journal* **2020**, *393*, No. 124796.

(26) Li, S.; Yang, M.; Wang, H.; Jiang, Y. Adsorption of microplastics on aquifer media: Effects of the action time, initial concentration, ionic strength, ionic types and dissolved organic matter. *Environ. Pollut.* **2022**, *308*, No. 119482.

(27) Cheng, Y.-R.; Wang, H.-Y. Highly effective removal of microplastics by microalgae Scenedesmus abundans. *Chemical Engineering Journal* **2022**, *435*, No. 135079.

(28) Yuan, F.; Yue, L.; Zhao, H.; Wu, H. Study on the adsorption of polystyrene microplastics by three-dimensional reduced graphene oxide. *Water Sci. Technol.* **2020**, *81*, 2163−2175.

(29) Heo, Y.; Lee, E.-H.; Lee, S.-W. Adsorptive removal of micron-sized polystyrene particles using magnetic iron oxide nanoparticles. *Chemosphere* **2022**, *307*, No. 135672.

(30) Sajid, M.; Ihsanullah, I.; Khan, M. T.; Baig, N. Nanomaterials-based adsorbents for remediation of microplastics and nanoplastics in aqueous media: A review. *Sep. Purif. Technol.* **2022**, No. 122453.

(31) Leslie, H. A.; Van Velzen, M. J.; Brandsma, S. H.; Vethaak, A. D.; Garcia-Vallejo, J. J.; Lamoree, M. H. Discovery and quantification of plastic particle pollution in human blood. *Environ. Int.* **2022**, *163*, No. 107199.

(32) Walker, T. R.; Fequet, L. Current trends of unsustainable plastic production and micro (nano) plastic pollution. *TrAC Trends in Analytical Chemistry* **2023**, *160*, No. 116984.

(33) Fu, L.; Li, J.; Wang, G.; Luan, Y.; Dai, W. Adsorption behavior of organic pollutants on microplastics. *Ecotoxicology and Environmental Safety* **2021**, *217*, No. 112207.

(34) Yu, Y.; Mo, W. Y.; Luukkonen, T. Adsorption behaviour and interaction of organic micropollutants with nano and microplastics—a review. *Sci. Total Environ.* **2021**, *797*, No. 149140.

(35) Costigan, E.; Collins, A.; Hatinoglu, M. D.; Bhagat, K.; MacRae, J.; Perreault, F.; Apul, O. Adsorption of organic pollutants by microplastics: Overview of a dissonant literature. *Journal of Hazardous Materials Advances* **2022**, *6*, No. 100091.

(36) Bhagat, K.; Barrios, A. C.; Rajwade, K.; Kumar, A.; Oswald, J.; Apul, O.; Perreault, F. Aging of microplastics increases their adsorption affinity towards organic contaminants. *Chemosphere* **2022**, *298*, No. 134238.

(37) Budhiraja, V.; Urh, A.; Horvat, P.; Krzan, A. Synergistic adsorption of organic pollutants on weathered polyethylene microplastics. *Polymers* **2022**, *14*, 2674.

(38) Li, J.; Zhang, K.; Zhang, H. Adsorption of antibiotics on microplastics. *Environ. Pollut.* **2018**, *237*, 460−467.

(39) Fu, Q.; Tan, X.; Ye, S.; Ma, L.; Gu, Y.; Zhang, P.; Chen, Q.; Yang, Y.; Tang, Y. Mechanism analysis of heavy metal lead captured by natural-aged microplastics. *Chemosphere* **2021**, *270*, No. 128624.

(40) Kinigopoulou, V.; Pashalidis, I.; Kalderis, D.; Anastopoulos, I. Microplastics as carriers of inorganic and organic contaminants in the environment: A review of recent progress. *J. Mol. Liq.* **2022**, *350*, No. 118580.

(41) Santana-Viera, S.; Montesdeoca-Esponda, S.; Guedes-Alonso, R.; Sosa-Ferrera, Z.; Santana-Rodríguez, J. J. Organic pollutants adsorbed on microplastics: Analytical methodologies and occurrence in oceans. *Trends in Environmental Analytical Chemistry* **2021**, *29*, No. e00114.

(42) Zhang, J.; Zhan, S.; Zhong, L.-B.; Wang, X.; Qiu, Z.; Zheng, Y.-M. Adsorption of typical natural organic matter on microplastics in aqueous solution: Kinetics, isotherm, influence factors and mechanism. *Journal of Hazardous Materials* **2023**, *443*, No. 130130.

(43) Chen, Z.; Yang, J.; Huang, D.; Wang, S.; Jiang, K.; Sun, W.; Chen, Z.; Cao, Z.; Ren, Y.; Wang, Q. Adsorption behavior of aniline

pollutant on polystyrene microplastics. *Chemosphere* **2023**, *323*, No. 138187.

(44) Hu, J.; Lim, F. Y.; Hu, J. Characteristics and behaviors of microplastics undergoing photoaging and Advanced Oxidation Processes (AOPs) initiated aging. *Water Res.* **2023**, *232*, No. 119628.

(45) Liu, R.; Wang, Y.; Yang, Y.; Shen, L.; Zhang, B.; Dong, Z.; Gao, C.; Xing, B. New insights into adsorption mechanism of pristine and weathered polyamide microplastics towards hydrophilic organic compounds. *Environ. Pollut.* **2023**, *317*, No. 120818.

(46) Tong, F.; Liu, D.; Zhang, Z.; Chen, W.; Fan, G.; Gao, Y.; Gu, X.; Gu, C. Heavy metal-mediated adsorption of antibiotic tetracycline and ciprofloxacin on two microplastics: Insights into the role of complexation. *Environmental Research* **2023**, *216*, No. 114716.

(47) Liu, W.; Pan, T.; Liu, H.; Jiang, M.; Zhang, T. Adsorption behavior of imidacloprid pesticide on polar microplastics under environmental conditions: Critical role of photo-aging. *Front. Environ. Sci. Eng.* **2023**, *17*, 41.

(48) Hatinoglu, M. D.; Perreault, F.; Apul, O. G. Modified linear solvation energy relationships for adsorption of perfluorocarboxylic acids by polystyrene microplastics. *Science of The Total Environment* **2023**, *860*, No. 160524.

(49) Naqash, N.; Prakash, S.; Kapoor, D.; Singh, R. Interaction of freshwater microplastics with biota and heavy metals: a review. *Environmental Chemistry Letters* **2020**, *18*, 1813−1824.

(50) Godoy, V.; Blázquez, G.; Calero, M.; Quesada, L.; Martín-Lara, M. The potential of microplastics as carriers of metals. *Environ. Pollut.* **2019**, *255*, No. 113363.

(51) Gao, X.; Hassan, I.; Peng, Y.; Huo, S.; Ling, L. Behaviors and influencing factors of the heavy metals adsorption onto microplastics: A review. *Journal of Cleaner Production* **2021**, *319*, No. 128777.

(52) Wang, L.; Guo, C.; Qian, Q.; Lang, D.; Wu, R.; Abliz, S.; Wang, W.; Wang, J. Adsorption behavior of UV aged microplastics on the heavy metals Pb (II) and Cu (II) in aqueous solutions. *Chemosphere* **2023**, *313*, No. 137439.

(53) Stapleton, M. J.; Ansari, A. J.; Hai, F. I. Antibiotic sorption onto microplastics in water: A critical review of the factors, mechanisms and implications. *Water Res.* **2023**, *233*, No. 119790.

(54) Verma, S.; Kim, K.-H.; Kumar, N.; Bhattacharya, S. S.; Naushad, M.; Dutta, R. K. Amine-amide functionalized graphene oxide sheets as bifunctional adsorbent for the removal of polar organic pollutants. *Journal of Hazardous Materials* **2022**, *429*, No. 128308.

(55) Modak, S.; Kasula, M.; Esfahani, M. R. Nanoplastics removal from water using metal−organic framework: investigation of adsorption mechanisms, kinetics, and effective environmental parameters. *ACS Applied Engineering Materials* **2023**, *1*, 744−755.

(56) Li, J.; Chen, X.; Yu, S.; Cui, M. Removal of pristine and aged microplastics from water by magnetic biochar: Adsorption and magnetization. *Science of The Total Environment* **2023**, *875*, No. 162647.

(57) Omorogie, M. O.; Babalola, J. O.; Unuabonah, E. I.; Gong, J. R. Clean technology approach for the competitive binding of toxic metal ions onto MnO 2 nano-bioextractant. *Clean Technologies and Environmental Policy* **2016**, *18*, 171−184.

(58) Omorogie, M. O.; Ilesanmi, F. O.; Alfred, M. O.; Helmreich, B. Thermally-treated MgO/nanocrystalline cellulose immobilized onto a Santa Barbara-16 mesoporous SiO 2 template for the sequestration of antibiotics from polluted water. *New J. Chem.* **2022**, *46*, 20918−20931.

(59) Ho, Y.-S.; Chiu, W.-T.; Wang, C.-C. Regression analysis for the sorption isotherms of basic dyes on sugarcane dust. *Bioresource technology* **2005**, *96*, 1285−1291.

(60) Langmuir, I. The constitution and fundamental properties of solids and liquids. Part I. Solids. *Journal of the American chemical society* **1916**, *38*, 2221−2295.

(61) Umpleby, R. J.; Baxter, S. C.; Chen, Y.; Shah, R. N.; Shimizu, K. D. Characterization of molecularly imprinted polymers with the Langmuir− Freundlich isotherm. *Analytical chemistry* **2001**, *73*, 4584−4591.

(62) Yuh-Shan, H. Citation review of Lagergren kinetic rate equation on adsorption reactions. *Scientometrics* **2004**, *59*, 171−177.

(63) Ho, Y.-S.; Ofomaja, A. E. Pseudo-second-order model for lead ion sorption from aqueous solutions onto palm kernel fiber. *Journal of hazardous materials* **2006**, *129*, 137−142.

(64) El Boundati, Y.; Ziat, K.; Naji, A.; Saidi, M. Generalized fractal-like adsorption kinetic models: Application to adsorption of copper on Argan nut shell. *J. Mol. Liq.* **2019**, *276*, 15−26.

(65) Njuguna, D. G.; Schönherr, H. Xanthan gum hydrogels as high-capacity adsorbents for dye removal. *ACS Applied Polymer Materials* **2021**, *3*, 3142−3152.

(66) Desmet, C.; Valsesia, A.; Oddo, A.; Ceccone, G.; Spampinato, V.; Rossi, F.; Colpo, P. Characterisation of nanomaterial hydrophobicity using engineered surfaces. *J. Nanopart. Res.* **2017**, *19*, 1−17.

(67) Saleem, A.; Chen, J.; Liu, M.; Liu, N.; Usman, M.; Wang, K.; Haris, M.; Zhang, Y.; Li, P. Versatile Magnetic Mesoporous Carbon Derived Nano-Adsorbent for Synchronized Toxic Metal Removal and Bacterial Disinfection from Water Matrices. *Small* **2023**, 2207348.

(68) Abdelsalam, E. M.; Samer, M.; Seifelnasr, A.; Moselhy, M. A.; Ibrahim, H. H.; Faried, M.; Attia, Y. A. Effects of Al2O3, SiO2 nanoparticles, and g-c3n4 nanosheets on biocement production from agricultural wastes. *Sci. Rep.* **2023**, *13*, 2720.

(69) Omorogie, M. O.; Babalola, J. O.; Unuabonah, E. I.; Song, W.; Gong, J. R. Efficient chromium abstraction from aqueous solution using a low-cost biosorbent: Nauclea diderrichii seed biomass waste. *Journal of Saudi Chemical Society* **2016**, *20*, 49−57.

(70) Özmeral, N.; Işık, M.; Sogancioglu Kalem, M.; Ahmetli, G. Lignocellulose coffee waste-based epoxy composites: effect of various treatment methods on composite properties. *Cellulose* **2023**, *30*, 3589−3609.

(71) Ben Abdallah, A.; Ben Hassen Trabelsi, A.; Navarro, M. V.; Veses, A.; García, T.; Mihoubi, D. Pyrolysis of tea and coffee wastes: effect of physicochemical properties on kinetic and thermodynamic characteristics. *J. Therm. Anal. Calorim.* **2023**, *148*, 2501−2515.

(72) Khenniche, L.; Saidou Souleymane, M.; Chemache, Z.; Benissad-Aissani, F.; Amrane, A. Single-step and two-step syntheses of magnetic carbons from coffee residue: elimination of sulfamethazine by adsorption. *International Journal of Environmental Science and Technology* **2023**, *20*, 755−768.

(73) Fernández, J. V.; Faria, D. N.; Santoro, M. C.; Mantovaneli, R.; Cipriano, D. F.; Brito, G. M.; Carneiro, M. T. W.; Schettino, M. A., Jr; Gonzalez, J. L.; Freitas, J. C. Use of Unmodified Coffee Husk Biochar and Ashes as Heterogeneous Catalysts in Biodiesel Synthesis. *BioEnergy Research* **2022**, 1−12.

(74) Wang, H.; Li, X.; Zhao, S.; Liu, Q.; Li, N.; Su, Z.; Ren, J.; Hao, X.; Peng, F. Repurposing Xylan Biowastes for Sustainable Household Detergents. *ACS Sustainable Chem. Eng.* **2023**, *11*, 2949−2958.

(75) Omorogie, M. O.; Babalola, J. O.; Ismaeel, M. O.; McGettrick, J. D.; Watson, T. M.; Dawson, D. M.; Carta, M.; Kuehnel, M. F. Activated carbon from Nauclea diderrichii agricultural waste—a promising adsorbent for ibuprofen, methylene blue and CO2. *Advanced Powder Technology* **2021**, *32*, 866−874.

(76) Gama, N.; Ferreira, A.; Evtuguin, D. V. New poly (lactic acid) composites produced from coffee beverage wastes. *J. Appl. Polym. Sci.* **2022**, *139*, 51434.

(77) Nurwahid, I. H.; Khalil, M.; Yunarti, R. T. The enhancement of specific capacitance of carbon derived from spent coffee grounds with SiO2 nanoparticles. *Chemical Papers* **2023**, *77*, 1669−1681.

(78) Omorogie, M. O.; Babalola, J. O.; Unuabonah, E. I.; Gong, J. R. Solid phase extraction of hazardous metals from aqua system by nanoparticle-modified agrowaste composite adsorbents. *Journal of Environmental Chemical Engineering* **2014**, *2*, 675−684.

(79) Li, Z.; Deng, L.; Kinloch, I. A.; Young, R. J. Raman spectroscopy of carbon materials and their composites: Graphene, nanotubes and fibres. *Prog. Mater. Sci.* **2023**, *135*, No. 101089.

(80) Eberle, A.; Greiner, A.; Ivleva, N. P.; Arumugam, B.; Niessner, R.; Trixler, F. Doping graphene via organic solid-solid wetting deposition. *Carbon* **2017**, *125*, 84−92.

(81) Lee, A. Y.; Yang, K.; Anh, N. D.; Park, C.; Lee, S. M.; Lee, T. G.; Jeong, M. S. Raman study of D* band in graphene oxide and its correlation with reduction. *Appl. Surf. Sci.* **2021**, *536*, No. 147990.

(82) Kumar, N.; Srivastava, V. C. Simple synthesis of large graphene oxide sheets via electrochemical method coupled with oxidation process. *ACS omega* **2018**, *3*, 10233−10242.

(83) Vieira, R. S.; Oliveira, M. L. M.; Guibal, E.; Rodríguez-Castellón, E.; Beppu, M. M. Copper, mercury and chromium adsorption on natural and crosslinked chitosan films: An XPS investigation of mechanism. *Colloids Surf., A* **2011**, *374*, 108−114.

(84) Zhang, X.; Yan, L.; Li, J.; Yu, H. Adsorption of heavy metals by l-cysteine intercalated layered double hydroxide: Kinetic, isothermal and mechanistic studies. *J. Colloid Interface Sci.* **2020**, *562*, 149−158.

(85) Xu, J.; Guo, Y.; Tang, C.; Qian, Y.; Guo, C.; Wang, Z.; Li, L. Hardwood vessel-inspired chitosan-based sponge with superior compressibility, superfast adsorption and remarkable recyclability for microplastics removal in water. *Chemical Engineering Journal* **2023**, *475*, No. 146130.

(86) Li, H.; Tang, M.; Wang, J.; Dong, L.; Wang, L.; Liu, Q.; Huang, Q.; Lu, S. Theoretical and experimental investigation on rapid and efficient adsorption characteristics of microplastics by magnetic sponge carbon. *Science of The Total Environment* **2023**, *897*, No. 165404.

(87) You, Z.; Liu, G.; Wang, L.; Zhang, X. Binderless nano-HZSM-5 zeolite coatings prepared through combining washcoating and dry-gel conversion (DGC) methods. *Microporous and mesoporous materials* **2013**, *170*, 235−242.

(88) Kim, J.; Kumar, N.; Jung, U.; Park, J.; Naushad, M. Enhanced photocatalytic activity of cubic ZnSn (OH) 6 by in-situ partial phase transformation via rapid thermal annealing. *Chemosphere* **2023**, *331*, No. 138780.

(89) Gerente, C.; Lee, V.; Cloirec, P. L.; McKay, G. Application of chitosan for the removal of metals from wastewaters by adsorption—mechanisms and models review. *Critical reviews in environmental science and technology* **2007**, *37*, 41−127.

(90) Önal, Y.; Akmil-Başar, C.; Sarıcı-Özdemir, Ç. Investigation kinetics mechanisms of adsorption malachite green onto activated carbon. *Journal of hazardous materials* **2007**, *146*, 194−203.

(91) Babalola, J. O.; Olayiwola, F. T.; Olowoyo, J. O.; Alabi, A. H.; Unuabonah, E. I.; Ofomaja, A. E.; Omorogie, M. O. Adsorption and desorption kinetics of toxic organic and inorganic ions using an indigenous biomass: Terminalia ivorensis seed waste. *International Journal of Industrial Chemistry* **2017**, *8*, 207−220.

(92) Dou, S.; Ke, X.-X.; Shao, Z.-D.; Zhong, L.-B.; Zhao, Q.-B.; Zheng, Y.-M. Fish scale-based biochar with defined pore size and ultrahigh specific surface area for highly efficient adsorption of ciprofloxacin. *Chemosphere* **2022**, *287*, No. 131962.

(93) Omorogie, M. O.; Naidoo, E. B.; Ofomaja, A. E. Response surface methodology, central composite design, process methodology and characterization of pyrolyzed KOH pretreated environmental biomass: mathematical modelling and optimization approach. *Modeling Earth Systems and Environment* **2017**, *3*, 1171−1186.

(94) Chen, S.; Qin, C.; Wang, T.; Chen, F.; Li, X.; Hou, H.; Zhou, M. Study on the adsorption of dyestuffs with different properties by sludge-rice husk biochar: adsorption capacity, isotherm, kinetic, thermodynamics and mechanism. *J. Mol. Liq.* **2019**, *285*, 62−74.

(95) Tran, H. N.; Tomul, F.; Ha, N. T. H.; Nguyen, D. T.; Lima, E. C.; Le, G. T.; Chang, C.-T.; Masindi, V.; Woo, S. H. Innovative spherical biochar for pharmaceutical removal from water: Insight into adsorption mechanism. *J. Hazard. Mater.* **2020**, *394*, No. 122255.

(96) Li, X.; Zhang, L.; Yang, Z.; Wang, P.; Yan, Y.; Ran, J. Adsorption materials for volatile organic compounds (VOCs) and the key factors for VOCs adsorption process: A review. *Sep. Purif. Technol.* **2020**, *235*, No. 116213.

(97) Brewer, C. E.; Chuang, V. J.; Masiello, C. A.; Gonnermann, H.; Gao, X.; Dugan, B.; Driver, L. E.; Panzacchi, P.; Zygourakis, K.; Davies, C. A. New approaches to measuring biochar density and porosity. *Biomass and bioenergy* **2014**, *66*, 176−185.

(98) Tan, X.-F.; Zhu, S.-S.; Wang, R.-P.; Chen, Y.-D.; Show, P.-L.; Zhang, F.-F.; Ho, S.-H. Role of biochar surface characteristics in the adsorption of aromatic compounds: Pore structure and functional groups. *Chin. Chem. Lett.* **2021**, *32*, 2939−2946.

(99) Huang, X.; Hadi, P.; Joshi, R.; Alhamzani, A. G.; Hsiao, B. S. A comparative study of mechanism and performance of anionic and cationic dialdehyde nanocelluloses for dye adsorption and separation. *ACS omega* **2023**, *8*, 8634−8649.

(100) Whitby, K. T.; Liu, B. Y. Polystyrene aerosols—electrical charge and residue size distribution. *Atmospheric Environment (1967)* **1968**, *2*, 103−116.

(101) Ofomaja, A. E. Sorptive removal of Methylene blue from aqueous solution using palm kernel fibre: Effect of fibre dose. *Biochemical Engineering Journal* **2008**, *40*, 8−18.

(102) Nandi, B.; Goswami, A.; Purkait, M. Removal of cationic dyes from aqueous solutions by kaolin: kinetic and equilibrium studies. *Appl. Clay Sci.* **2009**, *42*, 583−590.

(103) Fulazzaky, M. A.; Khamidun, M. H.; Omar, R. Understanding of mass transfer resistance for the adsorption of solute onto porous material from the modified mass transfer factor models. *Chemical Engineering Journal* **2013**, *228*, 1023−1029.

(104) Luo, D.; Wang, L.; Nan, H.; Cao, Y.; Wang, H.; Kumar, T. V.; Wang, C. Phosphorus adsorption by functionalized biochar: A review. *Environmental Chemistry Letters* **2023**, *21*, 497−524.

(105) Chen, X.; Hossain, M. F.; Duan, C.; Lu, J.; Tsang, Y. F.; Islam, M. S.; Zhou, Y. Isotherm models for adsorption of heavy metals from water-A review. *Chemosphere* **2022**, *307*, No. 135545.

(106) Huang, Z.; Bu, J.; Wang, H. Application of two modified kaolin materials in removing micro-plastics from water. *Journal of Material Cycles and Waste Management* **2022**, *24*, 1460−1475.

(107) Zandieh, M.; Liu, J. Removal and degradation of microplastics using the magnetic and nanozyme activities of bare iron oxide nanoaggregates. *Angew. Chem., Int. Ed.* **2022**, *61*, No. e202212013.

(108) Ganie, Z. A.; Khandelwal, N.; Tiwari, E.; Singh, N.; Darbha, G. K. Biochar-facilitated remediation of nanoplastic contaminated water: Effect of pyrolysis temperature induced surface modifications. *Journal of Hazardous Materials* **2021**, *417*, No. 126096.

(109) Arenas, L. R.; Gentile, S. R.; Zimmermann, S.; Stoll, S. Nanoplastics adsorption and removal efficiency by granular activated carbon used in drinking water treatment process. *Sci. Total Environ.* **2021**, *791*, No. 148175.